Hindawi Publishing Corporation
Journal of Nanomaterials
Volume 2012, Article ID 942801, 9 pages
doi:10.1155/2012/942801

Research Article

Synthesis, Structure, and Luminescent Properties of Europium-Doped Hydroxyapatite Nanocrystalline Powders

Carmen Steluta Ciobanu,[1] Simona Liliana Iconaru,[1] Florian Massuyeau,[2] Liliana Violeta Constantin,[3] Adrian Costescu,[3] and Daniela Predoi[1]

[1] *National Institute of Materials Physics, P.O. Box MG 07, 76900 Bucharest, Romania*
[2] *Institute des Materiaux Jean Rouxel, 02 rue de la Houssinière, P.O. Box 32 229, 44322 Nantes, France*
[3] *Faculty of Physics, University of Bucharest, 405 Atomistilor, P.O. Box MG-1, 077125 Bucharest, Romania*

Correspondence should be addressed to Daniela Predoi, dpredoi@gmail.com

Received 20 December 2011; Revised 22 February 2012; Accepted 23 February 2012

Academic Editor: Takuya Tsuzuki

The luminescent europium-doped hydroxyapatite (Eu:HAp, $Ca_{10-x}Eu_x(PO_4)_6(OH)_2$) with $0 \leq x \leq 0.2$ nanocrystalline powders was synthesized by coprecipitation. The structural, morphological, and textural properties were well characterized by X-ray diffraction, scanning electron microscopy, and transmission electron microscopy. The vibrational studies were performed by Fourier transform infrared, Raman, and photoluminescence spectroscopies. The X-ray diffraction analysis revealed that hydroxyapatite is the unique crystalline constituent of all the samples, indicating that Eu has been successfully inserted into the HAp lattice. Eu doping inhibits HAp crystallization, leading to a decrease of the average crystallite size from around 20 nm in the undoped sample to around 7 nm in the sample with the highest Eu concentration. Furthermore, the samples show the characteristic $^5D_0 \rightarrow {}^7F_0$ transition observed at 578 nm related to Eu^{3+} ions distributed on Ca^{2+} sites of the apatitic structure.

1. Introduction

Hydroxyapatite (HAp, $Ca_{10}(PO_4)_6(OH)_2$) belongs to the apatite family with general formula $Ca_{10}(PO_4)_6X_2$, X being a fluorine, chlorine ion, or a hydroxyl group. HAp being the major inorganic component in natural bones crystallizes in hexagonal system. Synthetic HAp has the same chemical composition as biological HAp and thus mimics many properties of natural bone [1–3]. On the other hand, synthetic HAp is limited in use due to high in vivo solubility and poor mechanical properties, such as low-impact resistance [4, 5]. The physical, chemical, and biological properties of HAp are controlled by its crystal structure and composition. Substitution of Ca^{2+} with other metal ions into the HAp structure is one of the effective ways to improve the properties of HAp. Metal ions such as Ag^+, Cu^{2+}, and Zn^{2+} in the HAp structure can affect its crystallinity, morphology, and lattice parameters. The advantages of doping HAp with foreign elements pertinent to orthopedic applications were reported by others. For example, Y-doped calcium oxyhydroxyapatite [6] has been studied for humidity sensor applications due to its high affinity for water molecules [7]. The doping of HAp with 2 mol% of Zn^{2+} significantly increased osteoblast adhesion [8]. Webster et al. [9] reported that the Bi^{3+} would be the best choice of dopant to enhance properties of HAp pertinent for bone implant applications.

Being an important emitter in the red region of the visible spectrum, Eu^{3+} ions have been utilized extensively in color television and high-efficiency fluorescent lamps [10, 11]. Therefore, Eu^{3+} ions have been widely used as a local structure probe [12–16]. Labeling using organic fluorescent molecules is popular in clinical use for years. In recent years, a lot of inorganic components even nanoparticles were suggested to be such candidates [15]. However, the toxicity of particles used is an important issue in practical application due to composition and nanosize nature. A luminescent agent with great biocompatibility is ideal for implantation and clinical application [16]. Particularly, in biomedicine

field, nanoparticles can be used as drug-delivery vehicles that can target tissues or cells [17] and can be functionalized with special characteristics (such as magnetization, fluorescence, and near-infrared absorption) for qualitative or quantitative detection of tumor cells [18]. As we know, the nanoscale fluorescent materials have attracted much interest due to the increasing demand for efficient photosensitive materials not only for sophisticated optoelectronic and photonic devices but also for a broad range of biomedical application [19]. In biomedical areas, the luminescent materials, mainly including fluorescent organic molecules [20, 21] and semiconductor nanoparticles [22, 23], have been widely investigated in biological staining and diagnostics. However, some serious problems of photobleaching and quenching of fluorescent organic molecules and the toxicity of semiconductor quantum dots are critically pronounced, which have seriously limited their applications in biomedical areas [23, 24]. Furthermore, high performance in function-specific biological applications requires that the composites possess some unique characteristics, such as uniform morphology, large surface areas, good dispersion, and so forth [24]. Recently, a class of the stable, efficient, and self-activated luminescent materials, whose emission is induced by the defects or impurities in the host lattices, has been prepared by various synthesis routes [25–28]. These novel self-activated inorganic materials may be a promising fluorescent material for biodetection due to their good optical properties and nontoxicity.

In this study, the objective towards this goal was to synthesize nanocrystalline HAp doped with Eu ions at low temperature and characterize their resulting properties. In this paper we investigate the doping of hydroxyapatite by europium ions and the influence of the atomic ratio Eu/(Eu + Ca) on the structure, morphology and optical properties. Europium-doped hydroxyapatite $Ca_{10-x}Eu_x(PO_4)_6(OH)_2$ with $0 \le x \le 0.2$ was synthesized by coprecipitation method at 100°C mixing $Eu(NO_3)_3 \cdot 6H_2O$, $Ca(NO_3)_2 \cdot 4H_2O$ and $(NH_4)_2HPO_4$ in deionized water. The structure, morphology, and vibrational and optical properties of the obtained samples were systematically characterized by X-ray diffraction (XRD), scanning electron microscopy (SEM), transmission electron microscopy (TEM), Fourier transform infrared (FT-IR), and FT-Raman spectroscopies. The powders were also characterized by steady-state photoluminescence.

2. Experimental

2.1. Sample Preparation. All the reagents for synthesis including ammonium dihydrogen phosphate $[(NH_4)_2HPO_4]$, calcium nitrate $[Ca(NO_3)_2 \cdot 4H_2O]$, and europium nitrate $[Eu(NO_3)_3 \cdot 6H_2O]$ (Alpha Aesare) were used as purchased, without purification.

Europium-doped hydroxyapatite (Eu:Hap, $Ca_{10-x}Eu_x(PO_4)_6(OH)_2$) nanoparticles were performed by setting $x = 0$ (HAp), $x = 0.01$ (HAp_E1), $x = 0.02$ (HAp_E2), $x = 0.1$ (Hap_E10), and $x = 0.2$ (HAp_E20) and [Ca + Eu]/P as 1.67. The $Eu(NO_3)_3 \cdot 6H_2O$ and $Ca(NO_3)_2 \cdot 4H_2O$ were dissolved in deionised water to obtain 300 mL [Ca + Eu]-containing solution. On the other hand the $(NH_4)_2HPO_4$ was dissolved in deionised water to make 300 mL P-containing solution. The [Ca + Eu]-containing solution was put into a Berzelius and stirred at 100°C during 30 minutes. Meanwhile the pH of P-containing solution was adjusted to 10 with NH_3 and stirred continuously for 30 minutes. The P-containing solution was added drop by drop into the [Ca + Eu]-containing solution and stirred for 2 h and the pH was constantly adjusted and kept at 10 during the reaction. After the reaction the deposited mixtures were washed several times with deionised water. The resulting material was dried at 100°C for 72 h.

3. Sample Characterization

3.1. X-Ray Diffraction (XRD). The samples were characterized by X-ray diffraction using a Bruker D8-Advance X-ray diffractometer, in powder setting, equipped with copper target X-ray tube, Ni filter, and a high-efficiency linear detector of Lynx Eye type, operated in integration mode. The patterns were scanned in the 2θ range 15–140°, with a step size of 0.02° and 36 s measuring time per step.

3.2. Scanning Electron Microscopy (SEM). The structure and morphology of the samples were studied using a HITACHI S2600N-type scanning electron microscope (SEM), operating at 25 kV in vacuum. The SEM studies were performed on powder samples. For the elemental analysis the electron microscope was equipped with an energy dispersive X-ray attachment (EDAX/2001 device).

3.3. Transmission Electron Microscopy (TEM). Studies were carried out using a JEOL 200 CX. The specimen for TEM imaging was prepared from the particles suspension in deionised water. A drop of well-dispersed supernatant was placed on a carbon-coated 200 mesh copper grid, followed by drying the sample at ambient conditions before it is attached to the sample holder on the microscope.

3.4. FT-IR Spectroscopy. The functional groups present in the prepared powder and in the powders calcinated at different temperatures were identified by FTIR (Spectrum BX Spectrometer). For this 1% of the powder was mixed and ground with 99% KBr. Tablets of 10 mm diameter for FTIR measurements were prepared by pressing the powder mixture at a load of 5 tons for 2 min, and the spectrum was taken in the range of 400 to 4000 cm^{-1} with resolution 4 and 128 times scanning.

3.5. Raman Spectroscopy. Raman studies were performed in a backscattering geometry, under laser excitation wavelengths 1064 nm, using a RFS 100 FT-Raman Bruker spectrophotometer.

3.6. Steady-State Photoluminescence (PL). Steady-state photoluminescence spectra are collected from the front-face geometry of the samples with a Jobin-Yvon Fluorolog spectrometer using a xenon lamp (500 W) as an excitation source.

Table 1: Calculated lattice constants and the deviation for Eu:Hap, $Ca_{10-x}Eu_x(PO_4)_6(OH)$ with different x values ($0 \le x \le 0.2$).

Samples	$a = b$/deviation (nm)	c/deviation (nm)	Doping concentration (%)
JCPDS 9-0432	0.9418	0.6884	
HAp	0.9417/0.0001	0.6883/0.0001	0
Hap_E1	0.9417/0.0001	0.6883/0.0001	1
Hap_E2	0.9416/0.0002	0.6881/0.0003	2
Hap_E10	0.9412/0.0006	0.6879/0.0005	10
Hap_E20	0.9409/0.0009	0.6878/0.0006	20

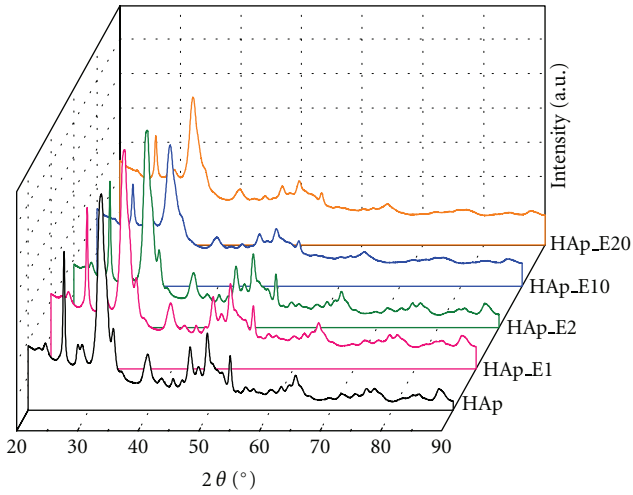

Figure 1: The XRD patterns of HAp and Eu:Hap, $Ca_{10-x}Eu_x(PO_4)_6(OH)_2$ samples synthesized with $0 \le x \le 0.2$.

4. Results and Discussions

The XRD patterns of the Eu:Hap, $Ca_{10-x}Eu_x(PO_4)_6(OH)_2$ nanoparticles prepared with different x values ($0 \le x \le 0.2$) are shown in Figure 1. It is obvious that all the XRD diffractions of each sample can be well indexed as a pure hexagonal phase ($P6_3/m$ space group), agreeing well with the values of the standard data (JCPDS no. 9-0432). In the case of the samples with $x \neq 0$, the characteristic diffractions of hexagonal HAp ($x = 0$) are still obvious, and no other phases related with doped component can be detected.

The samples with $x = 0.01$ (HAp_E1) and $x = 0.02$ (HAp_E2) are almost identical from XRD point of view with the undoped HAp ($x = 0$), showing very small differences concerning the relative intensities of the peaks. Furthermore, for $x = 0.1$ and $x = 0.2$, it can be found that the relative intensities of the diffractions decrease with the increasing of the Eu concentration, suggesting that the doping inhibits the HAp crystal growth. Besides, the fluorescence of Eu excited by the absorption of $Cu_{K\alpha}$ radiation on the Eu L shell may contribute substantially to this increased background intensity. (The cross section of the photoelectric effect is quite large (412.5 cm^2/g) because the L absorption edges of Eu, E_{EuL2} = 7.617 KeV and E_{EuL3} = 6.977 KeV, approaches the $Cu_{K\alpha}$ radiation energy used for analysis ($E_{CuK\alpha}$ = 8.049 KeV) [29]). The deviations of the relative intensities of the diffraction peaks from the reference are more visible in the pattern of the sample with the highest Eu concentration. Insightful analyses of the doped HAp structures, carried out by Rietveld whole-powder pattern fitting using the MAUD code [30], showed that Eu enters the HAp lattice by substituting Ca, with comparable probabilities for the two crystallographic sites of calcium in the HAp unit cell. The lattice parameters did not modify significantly after substitution. The XRD analysis using the anisotropic microstructure analysis implemented in MAUD as "Popa rules" [31] shows that the calculated lattice constants for Hap:Eu are in good agreement with the standard data of $a = b = 0.9418$ nm, $c = 0.6884$ nm. The unit-cell parameters of the corresponding samples are summarized in Table 1; the standard data of the JCPDS no. 9-0432 for hydroxyapatite are presented for comparison.

Figure 2 displays the TEM images of pure HAP ($x = 0$) and Eu:HAp ($0.01 \le x \le 0.2$) with low resolution and selected areas electron diffraction (SAED). Figures 2(a), 2(c), 2(e), and 2(g) presents TE micrograph of the Eu:HAp with low resolution for different values of x. Figures 2(b), 2(d), 2(f), and 2(h) shows selected areas electron diffraction (SAED) pattern of the synthesized powder, which confirms its crystallinity. As shown in Figures 2(a), 2(c), 2(e), and 2(g), all the samples exhibit a rod-like morphology which is consistent with the SEM results.

It can be seen from the HRTEM image of Eu:HAp with atomic ratio Eu/[Eu + Ca] = 20% (Figure 3) that the crystalline phase of hydroxyapatite with well-resolved lattice fringes can be observed. The distances (2.82 Å and 2.72 Å) between the adjacent lattice fringes agree well with the d_{211} and d_{004} spacing of the literature values (0.2814 nm and 0.2778 nm; CJPDS no. 09-0432).

The HRTEM images of the sample further confirm that the synthesized samples are well-crystallized single crystals.

The SEM images and EDS analysis of Eu:HAp samples prepared at the different atomic ratio Eu/[Eu + Ca] are displayed in Figure 4.

SEM images provide the direct information about the size and typical shapes of the prepared samples. It is found that all the samples Eu:HAp consists of relatively uniform rod-like particles. The result suggests that the doping Eu^{3+} has little influence on the morphology. These materials present quite different morphology, which reveals a homogeneous aspect of the synthesized particles for all samples. The samples prepared at the atomic ratio Eu/[Eu + Ca] 2% exhibit smaller particle size. When the atomic

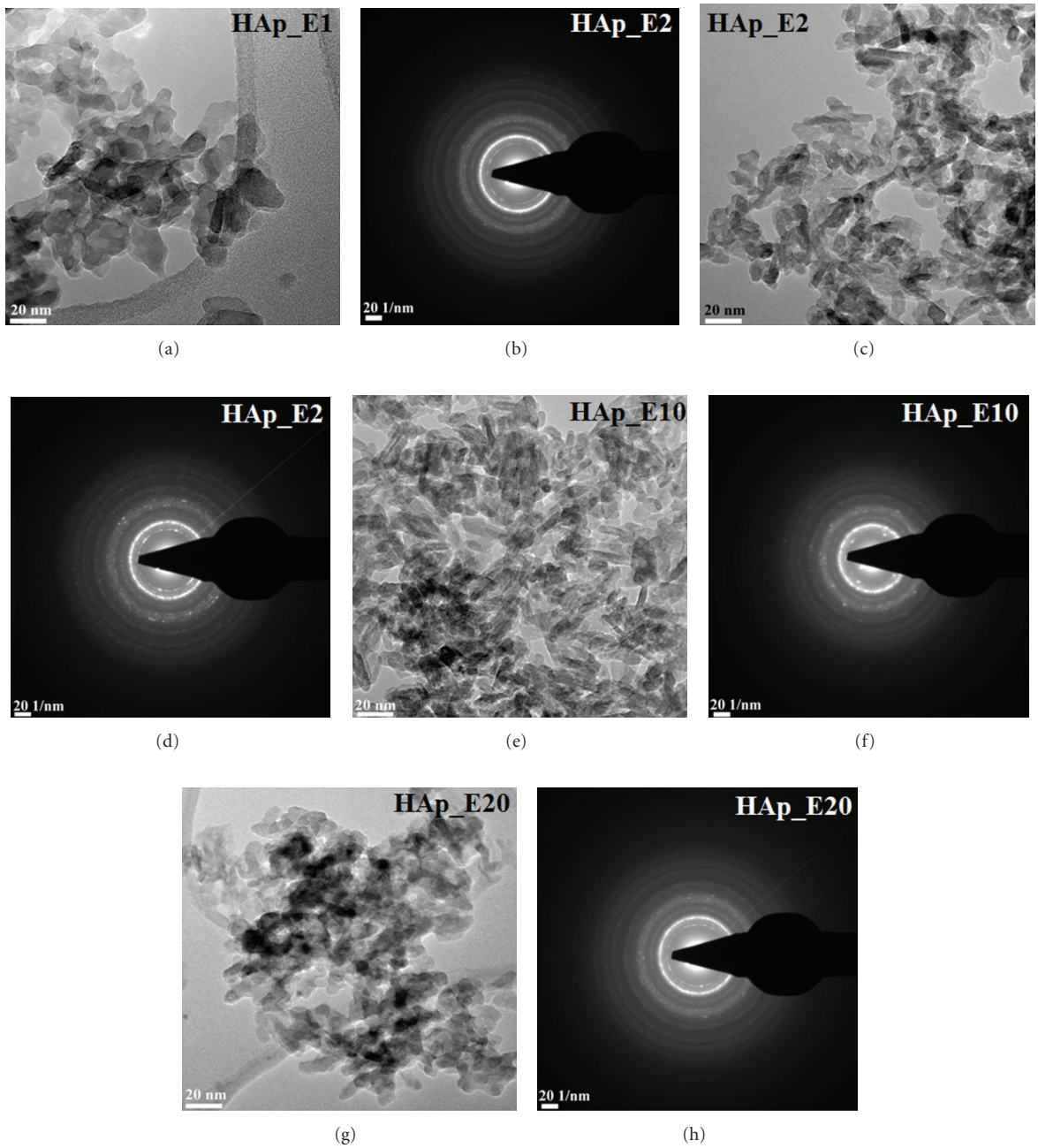

Figure 2: TEM images and SAED micrographies of the Eu:HAp samples synthesized with different ratio of Eu/(Ca + Eu) = 1% (Hap_E1), 2% (HAp_E2), 10% (HAp_E10), and 20% (HAp_E20).

ratio Eu/[Eu + Ca] is increased to 20%, the size of particles is smaller. The EDS spectrum (Figures 4(b), 4(d), 4(f), and 4(h)) of Eu:HAp confirms the presence of calcium (Ca), phosphorus (P), oxygen (O), and europium (Eu) in the Eu:HAp samples.

Figure 5 shows the FT-IR results obtained from Eu:HAp, when the atomic ratio Eu/(Ca + Eu) increases from 1 to 20%. For all the samples the presence of strong OH vibration peak (632 cm^{-1}) could be noticed. The broad bands in the regions 1600–1700 cm^{-1} and 3200–3600 cm^{-1} correspond to H–O–H bands of lattice water [32–34].

The strong absorption bands at 3429 cm^{-1} can be assigned to OH and H_2O for all the samples. Bands characteristics of the phosphate and hydrogen phosphate groups in apatitic environment were observed: 565 cm^{-1}, 632 cm^{-1}, 603 cm^{-1}, 962 cm^{-1}, and 1000–1100 cm^{-1} for the PO_4^{3-} groups [35, 36] and at 875 cm^{-1} for the HPO_4^{2-} ions. The bands at 1093 and 1033 cm^{-1} can be attributed to the triply degenerated ν_3 antisymmetric stretching of P–O band. The 962 cm^{-1} band can be due to the ν_1 non-degenerated symmetric stretching of P–O band. The bands at 603 cm^{-1} and 565 cm^{-1} are associated with the triply degenerated

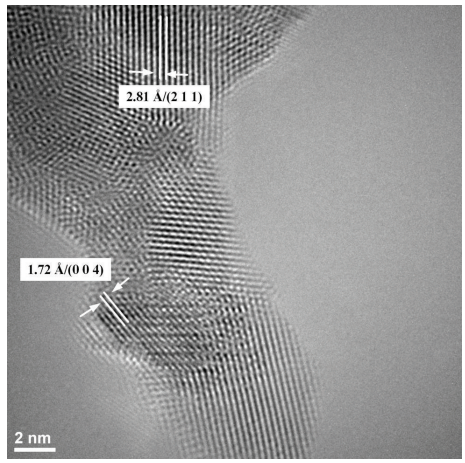

Figure 3: HRTEM image of Eu:HAp with ratio of Eu/(Eu + Ca) = 20%.

ν_4 vibration of O–P–O bond, and the bands at 475 cm^{-1} may be related with the doubly degenerated ν_2 bending of O–P–O bond. Moreover, it should be noted that the HPO_4^{2-} band was present in all the spectra, even for high values of Eu/(Ca + Eu) atomic ratio. The CO_3^{2-} band was presented in the spectra with atomic ratio Eu/(Ca + Eu) higher than 10% at 1400 cm^{-1} and 1508 cm^{-1} [3], respectively. The intensity of vibration peak decreases with the increasing of the Eu concentration. A broadening of peak vibration with the decreasing of the Eu concentration is also observed. These resultants suggest that the amounts of specific surface area of Eu:Hap increased with the Eu concentration. This compartment was observed by Owada et al. [6] in sintered Y-doped hydroxyapatite.

Complementary information can be obtained from Raman spectroscopy (Figure 6). The internal modes of the PO_4^{3-} tetrahedral ν_1 frequency (960 cm^{-1}) correspond to the symmetric stretching of P–O bonds. The vibrational bands at 429 cm^{-1} (ν_2), 450 cm^{-1} (ν_2) is attributed to the O–P–O bending modes.

We assigned the bands present at 1046 cm^{-1} (ν_3) and 1074 cm^{-1} (ν_3) to asymmetric ν_3(P–O) stretching. ν_4 (589 cm^{-1} and 608 cm^{-1}) can be addressed mainly to O–P–O bending character [3]. However, the intensity of vibration peak decreases when the atomic ratio Eu/(Ca + Eu) increases.

The PL properties of the sample were further characterized by the PL excitation and emission spectra, as shown in Figures 7 and 8. The excitation spectrum was obtained by the Eu^{3+} $^5D_0 \rightarrow {}^7F_2$ transition at 614 nm (Figure 7). In these excitation spectra, some sharp peaks originating from the f-f transitions of Eu^{3+} can be observed at 300 nm [37]. The highest excitation peaks are observed at 250 nm and 398 nm, in the UV region. Besides, excitation in the visible region is possible at 454 nm. The broad peak at 250 nm was attributed to a charge transfer transition between Eu^{3+} and O^{2-} [38, 39]. In the longer wavelength region, the weak peaks may arise from the direct excitation of the Eu^{3+} ground state into higher levels in the $4f^6$ configuration, which can be assigned to $^7F_0 \rightarrow {}^5H_6$ (320 nm), $^7F_0 \rightarrow {}^5D_4$ (365 nm), $^7F_0 \rightarrow {}^5G_2$ (382 nm), $^7F_0 \rightarrow {}^5L_6$ (398 nm), $^7F_0 \rightarrow {}^5D_3$ (421 nm), $^7F_0 \rightarrow {}^5D_2$ (454 nm), respectively [38].

Upon excitation at 394 nm, the characteristic transition lines from the excited $^5D_0$ level of Eu^{3+} ions can be detected in the emission spectra [40], as shown in Figure 8, and the locations of the emission lines with their assignments are labeled as well. Spectral features are observed in three different ranges: 570–582, 582–603, and 603–640 nm. They were ascribed to the $^5D_0 \rightarrow {}^7F_0$, $^5D_0 \rightarrow {}^7F_1$, and $^5D_0 \rightarrow {}^7F_2$ transitions, respectively. The $^5D_0 \rightarrow {}^7F_0$ transition observed at 578 nm is related to Eu^{3+} ions distributed on Ca^{2+} sites of the apatitic structure [1]. The two main characteristic peaks from $^5D_0 \rightarrow {}^7F_1$ (591 nm) and $^5D_0 \rightarrow {}^7F_2$ (614 nm) are dominant. The more efficient emission was observed for the hypersensitive $^5D_0$–$^7F_2$ transitions whose maximum intensity was obtained at 614 nm. PL intensity increased with increasing Eu doping concentration, and no significant modification of emission spectra was observed. It is worth noting that the characteristic emission lines are obvious in the emission spectra for all the spectra, showing the potential application to be tracked or monitored by the luminescence. The selective observations were made for excitation at the respective $^5D_0 \rightarrow {}^7F_0$ transition. For the $^5D_1$ level, three bands were observed in agreement with data reported for Eu^{3+}:$Sr_5(PO_4)_3F$ [41]. The assignment of the $^7F_1$ and $^7F_2$ components corresponds to those given by Vooronko et al. [42] in their study on Eu^{3+}:$Ca_5(PO_4)_3F$. A coupled substitution Ca^{2+}, $PO_4^{3-} \leftrightarrow Ln^{3+}$, SiO_4^{4-} has been proposed by other authors to explain the replacement of calcium by a rare earth Ln^{3+} in apatites [43, 44]. Such processes could not occur in our experimental conditions (absence of Na+ or SiO_4^{4-} ions). Lin et al. [45] in their studies on CeHAp with x_{Ce} from 0 to 0.2 have shown that cerium can partially substitute for calcium and enters the structure of HAp. In this case, after substitution, the crystallinity and the IR wavenumbers of bonds in CeHAp nanoparticles decreased gradually with the increased of x, and the morphology of the nanoparticles changed from the rod-shaped Hap to the needle-shaped CeHAp.

To the best of our knowledge, this is the first paper that demonstrates Eu-doped nanocrystalline hydroxyapatite by coprecipitation method at low temperature. Our studies show that the morphology of the nanoparticles does not change when the ratio of Eu/(Ca + Eu) increases. To determine the influence of Eu concentration on cell functions, drug loading, and release properties, future studies on this topic would be of significance for the development of materials and the design of bioceramics.

5. Conclusions

The aim of this work was to study the impact of the atomic ratio of Eu/(Ca + Eu) on the structural, morphological, and vibrational properties of hydroxyapatite nanocrystalline powders. In summary, a simple coprecipitation method has been developed to synthesize luminescent Eu^{3+} doped hydroxyapatite nanoparticles. We have synthesized europium-doped hydroxyapatite nanoparticles by coprecipitation method at low temperature with the atomic ratio

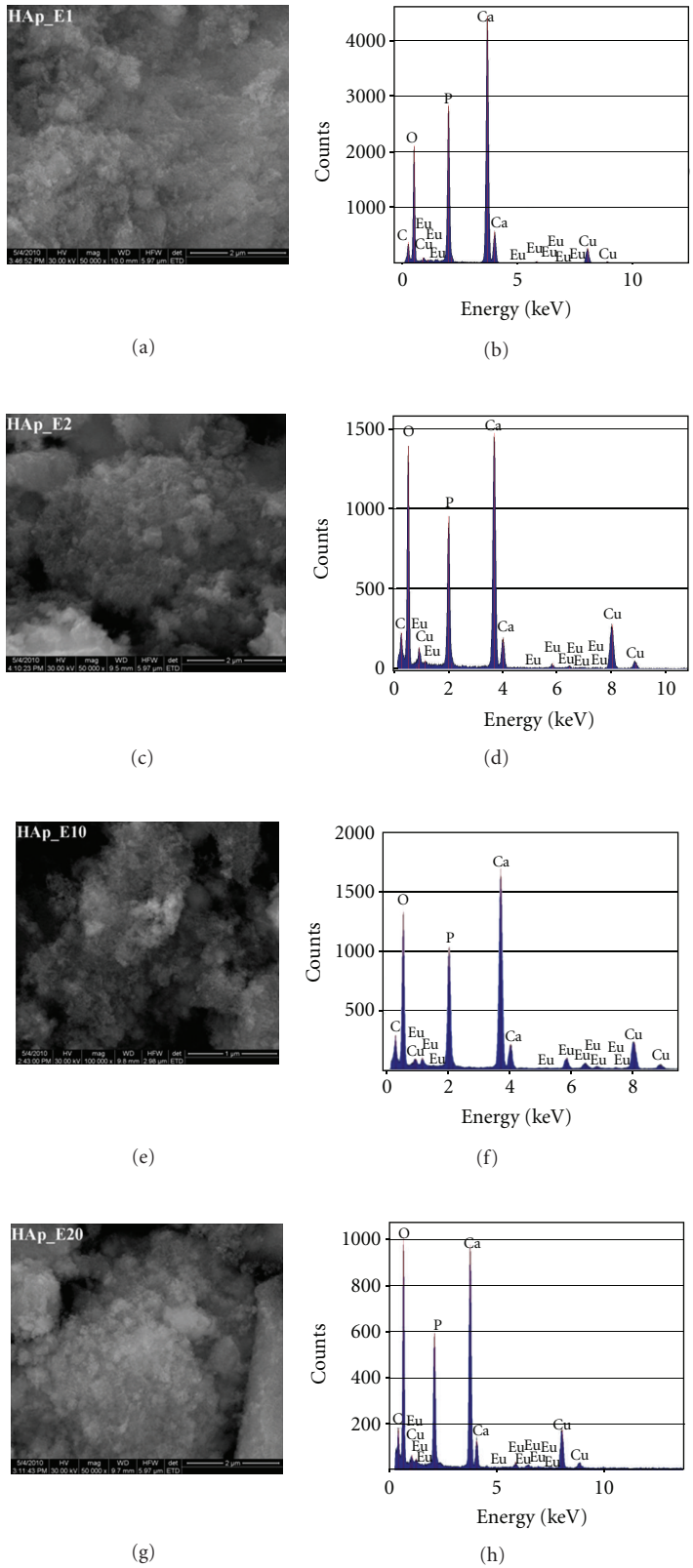

Figure 4: SEM images and the EDS of the Eu:HAp samples synthesized with Eu/(Ca + Eu) = 1% (Hap_E1), 2% (HAp_E2), 10% (HAp_E10) and 20% (HAp_E20).

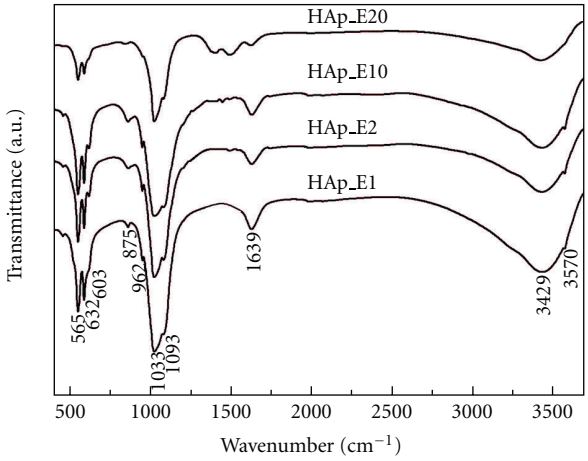

Figure 5: Transmittance infrared spectra of the Eu:HAp samples synthesized with Eu/(Ca+Eu) = 1%, 2%, 10%, and 20%.

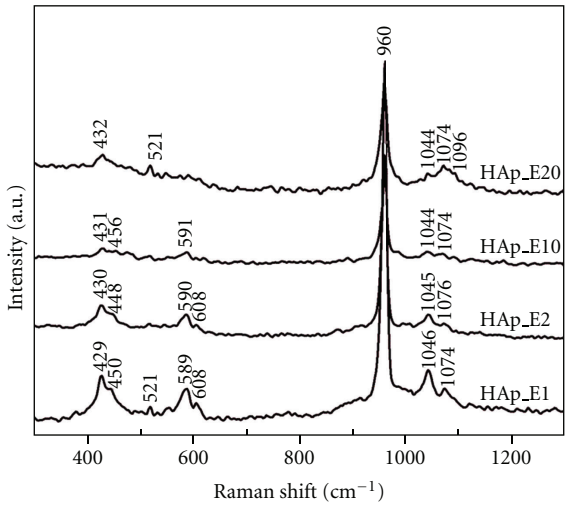

Figure 6: Raman spectra of the Eu:HAp samples synthesized with Eu/(Ca + Eu) = 1%, 2%, 10%, and 20%.

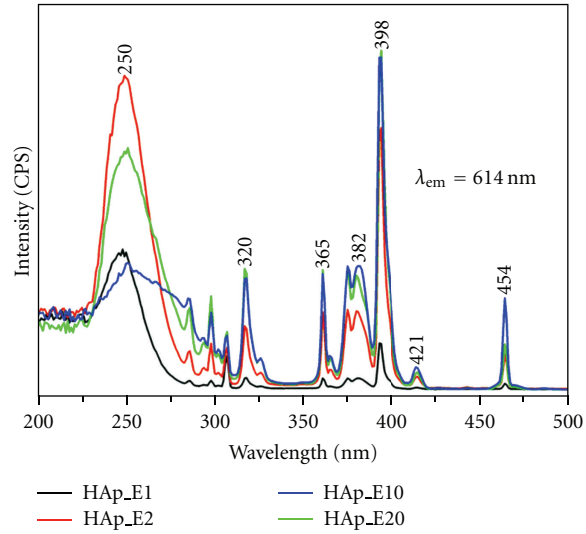

Figure 7: Excitation spectra of the Eu:HAp samples synthesized with Eu/(Ca + Eu) = 1%, 2%, 10%, and 20%.

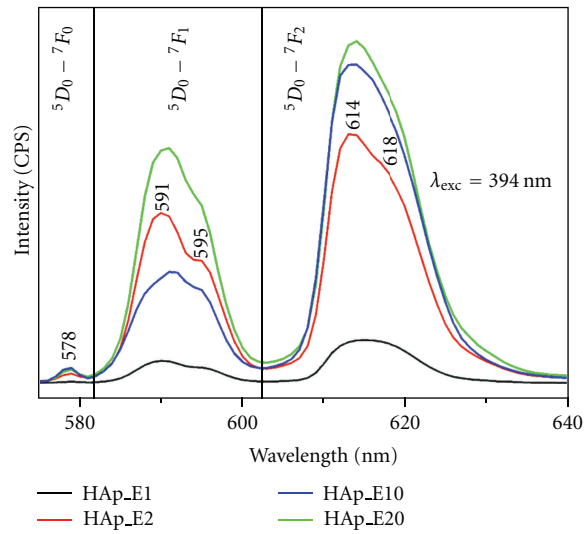

Figure 8: Emission spectra of the Eu:HAp samples synthesized with Eu/(Ca + Eu) = 1%, 2%, 10%, and 20%.

Eu/(Ca + Eu) = 1%, 2%, 10%, and 20%. The DRX studies have shown that Eu^{3+} has been successfully doped into HAp. The results reveal that the obtained pure HAp and Eu:HAp particles are well assigned to the hexagonal lattice structure of the hydroxyapatite phase. The as-prepared Eu:HAp samples conserve regular ellipsoidal morphology, and the doping Eu^{3+} has little influence on the morphology. The samples prepared at the atomic ratio Eu/[Eu + Ca] 20% exhibit much smaller average particle size then the materials with lower Eu content. In the PL spectrum the $^5D_0 \rightarrow {}^7F_0$ transition observed at 578 nm is related to Eu^{3+} ions distributed on Ca^{2+} sites of the apatitic structure. Furthermore, the photoluminescence intensities of the samples increase with the atomic ratio of Eu/(Ca + Eu). These studies demonstrate that luminescent Eu^{3+}-doped hydroxyapatite represents a potential application for drug release and targeting based on their luminescent properties. These results and methods could be interesting for academic and industry researchers in biomaterials, medical materials, and drug carriers.

Acknowledgment

This work was financially supported by the Science and Technology Ministry of Romania.

References

[1] M. E. Fleet and Y. Pan, "Site preference of Nd in fluorapatite [$Ca_{10}(PO_4)_6F_2$]," *Journal of Solid State Chemistry*, vol. 112, no. 1, pp. 78–81, 1994.

[2] M. E. Fleet and Y. Pan, "Site preference of rare earth elements in fluorapatite," *American Mineralogist*, vol. 80, no. 3-4, pp. 329–335, 1995.

[3] M. Mikou, A. Taitai, and J. L. Lacout, "On the dioxyapatites containing two rare-earth ions," *Annales de Chimie*, vol. 10, no. 7, pp. 645–651, 1985.

[4] M. Jarcho, "Retrospective analysis of hydroxyapatite development for oral implant applications," *Dental Clinics of North America*, vol. 36, no. 1, pp. 19–26, 1992.

[5] R. Knubovets, "Structural mineralogy and properties of natural phosphates," *Reviews in Chemical Engineering*, vol. 9, no. 3-4, pp. 161–216, 1993.

[6] H. Owada, K. Yamashita, T. Umegaki, T. Kanazawa, and M. Nagai, "Humidity-sensitivity of yttrium substituted apatite ceramics," *Solid State Ionics*, vol. 35, no. 3-4, pp. 401–404, 1989.

[7] R. E. Newnham, "Electroceramics," *Reports on Progress in Physics*, vol. 52, no. 2, pp. 123–156, 1989.

[8] T. J. Webster, C. Ergun, R. H. Doremus, and R. Bizios, "Hydroxylapatite with substituted magnesium, zinc, cadmium, and yttrium—II. Mechanisms of osteoblast adhesion," *Journal of Biomedical Materials Research*, vol. 59, no. 2, pp. 312–317, 2002.

[9] T. J. Webster, E. A. Massa-Schlueter, J. L. Smith, and E. B. Slamovich, "Osteoblast response to hydroxyapatite doped with divalent and trivalent cations," *Biomaterials*, vol. 25, no. 11, pp. 2111–2121, 2004.

[10] R. Ternane, M. Trabelsi-Ayedi, N. Kbir-Ariguib, and B. Piriou, "Luminescent properties of Eu^{3+} in calcium hydroxyapatite," *Journal of Luminescence*, vol. 81, no. 3, pp. 165–170, 1999.

[11] A. A. Bol and A. Meijerink, "Long-lived Mn^{2+} emission in nanocrystalline ZnS:Mn^{2+}," *Physical Review B*, vol. 58, no. 24, pp. R15997–R16000, 1998.

[12] N. Murase, R. Jagannathan, Y. Kanematsu et al., "Preparation and fluorescence properties of Eu^{3+}-doped strontium chloroapatite nanocrystals," *Journal of Luminescence*, vol. 87, pp. 488–490, 2000.

[13] R. Ternane, G. Panczer, M. T. Cohen-Adad et al., "Relationships between structural and luminescence properties in Eu^{3+}-doped new calcium borohydroxyapatite," *Optical Materials*, vol. 16, no. 1-2, pp. 291–300, 2001.

[14] A. Doat, M. Fanjul, F. Pellé, E. Hollande, and A. Lebugle, "Europium-doped bioapatite: a new photostable biological probe, internalizable by human cells," *Biomaterials*, vol. 24, no. 19, pp. 3365–3371, 2003.

[15] A. Doat, F. Pellé, and A. Lebugle, "Europium-doped calcium pyrophosphates: allotropic forms and photoluminescent properties," *Journal of Solid State Chemistry*, vol. 178, no. 7, pp. 2354–2362, 2005.

[16] A. Doat, F. Pellé, N. Gardant, and A. Lebugle, "Synthesis of luminescent bioapatite nanoparticles for utilization as a biological probe," *Journal of Solid State Chemistry*, vol. 177, no. 4-5, pp. 1179–1187, 2004.

[17] F. H. Chen, Q. Gao, and J. Z. Ni, "The grafting and release behavior of doxorubincin from Fe_3O_4@SiO_2 core-shell structure nanoparticles via an acid cleaving amide bond: the potential for magnetic targeting drug delivery," *Nanotechnology*, vol. 19, no. 16, Article ID 165103, 2008.

[18] D. Shi, "Integrated multifunctional nanosystems for medical diagnosis and treatment," *Advanced Functional Materials*, vol. 19, no. 21, pp. 3356–3373, 2009.

[19] P. R. Diamente, R. D. Burke, and F. C. J. M. Van Veggel, "Bioconjugation of Ln^{3+}-doped LaF3 nanoparticles to avidin," *Langmuir*, vol. 22, no. 4, pp. 1782–1788, 2006.

[20] J. Kim, H. S. Kim, N. Lee et al., "Multifunctional uniform nanoparticles composed of a magnetite nanocrystal core and a mesoporous silica shell for magnetic resonance and fluorescence imaging and for drug delivery," *Angewandte Chemie*, vol. 47, no. 44, pp. 8438–8441, 2008.

[21] A. Zumbuehl, D. Jeannerat, D. D. Clark et al., "An amphotericin B-fluorescein conjugate as a powerful probe for biochemical studies of the membrane," *Angewandte Chemie*, vol. 43, no. 39, pp. 5181–5185, 2004.

[22] X. Gao and S. Nie, "Molecular profiling of single cells and tissue specimens with quantum dots," *Trends in Biotechnology*, vol. 21, no. 9, pp. 371–373, 2003.

[23] K. T. Yong, H. Ding, I. Roy et al., "Imaging pancreatic cancer using bioconjugated inp quantum dots," *ACS Nano*, vol. 3, no. 3, pp. 502–510, 2009.

[24] P. Yang, Z. Quan, Z. Hou et al., "A magnetic, luminescent and mesoporous core-shell structured composite material as drug carrier," *Biomaterials*, vol. 30, no. 27, pp. 4786–4795, 2009.

[25] O. Parkash, B. Yadav, P. Singh, and D. Kumar, "Barrier layers formation in tin substituted calcium copper titanate $CaCu_3Ti_{4-x}Sn_xO_{12}$ ($0 \leq x \leq 1.0$)," *Journal of the Physical Society of Japan*, vol. 75, no. 9, Article ID 094717, 2006.

[26] D. Predoi, S. Derible, and H. Duflo, "Synthesis and ultrasonic characterization of hydroxyapatite ceramic powders," *Journal of Optoelectronics and Advanced Materials*, vol. 11, no. 6, pp. 852–856, 2009.

[27] D. Predoi, R. A. Vatasescu-Balcan, I. Pasuk, R. Trusca, and M. Costache, "Calcium phosphate ceramics for biomedical applications," *Journal of Optoelectronics and Advanced Materials*, vol. 10, no. 8, pp. 2151–2155, 2008.

[28] K. Kamishima, Y. Nagashima, K. Kakizaki et al., "Simple process synthesis of $BaTiO_3$-(Ni,Zn,Cu)Fe_2O_4 ceramic composite," *Journal of the Physical Society of Japan*, vol. 77, no. 6, Article ID 064801, 2008.

[29] P. Bandyopadhyay, X-ray periodic table, 1969.

[30] L. Lutterotti, "Total pattern fitting for the combined size-strain-stress-texture determination in thin film diffraction," *Nuclear Instruments and Methods in Physics Research Section B*, vol. 268, no. 3-4, pp. 334–340, 2010.

[31] N. C. Popa, "The (hkl) dependence of diffraction-line broadening caused by strain and size for all Laue groups in rietveld refinement," *Journal of Applied Crystallography*, vol. 31, no. 2, pp. 176–180, 1998.

[32] D. Predoi, R. V. Ghita, F. Ungureanu, C. C. Negrila, R. A. Vatasescu-Balcan, and M. Costache, "Characteristics of hydroxyapatite thin films," *Journal of Optoelectronics and Advanced Materials*, vol. 9, no. 12, pp. 3827–3831, 2007.

[33] D. Predoi, M. Barsan, E. Andronescu, R. A. Vatasescu-Balcan, and M. Costache, "Hydroxyapatite-iron oxide bioceramic prepared using nano-size powders," *Journal of Optoelectronics and Advanced Materials*, vol. 9, no. 11, pp. 3609–3613, 2007.

[34] A. Costescu, I. Pasuk, F. Ungureanu et al., "Physico-chemical properties of nano-sized hexagonal hydroxyapatite powder synthesized by sol-gel," *Digest Journal of Nanomaterials and Biostructures*, vol. 5, no. 4, pp. 989–1000, 2010.

[35] C. S. Ciobanu, E. Andronescu, A. Stoicu et al., "Influence of annealing treatment of nano-hydroxyapatite bioceramics on the vibrational properties," *Digest Journal of Nanomaterials and Biostructures*, vol. 6, no. 2, pp. 609–624, 2011.

[36] F. Frumosu, S. L. Iconaru, and D. Predoi, "Europium concentration effect of europium doped hydroxyapatite on proliferation of osteoblast cells," *Digest Journal of Nanomaterials and Biostructures*, vol. 6, no. 4, pp. 1859–1865, 2011.

[37] G. Blasse and B. C. Grabmaier, *Luminescent Materials*, Springer, Berlin, Germany, 1994.

[38] Y. Wang, X. Guo, T. Endo, Y. Murakami, and M. Ushirozawa, "Identification of charge transfer (CT) transition in (Gd,Y)BO 3:Eu phosphor under 100-300 nm," *Journal of Solid State Chemistry*, vol. 177, no. 7, pp. 2242–2248, 2004.

[39] C. X. Li, Z. W. Quan, J. Yang, P. Yang, and J. Lin, "Highly uniform and monodisperse β-$NaYF_4$: Ln^{3+} (Ln = Eu, Tb, Yb/Er, and Yb/Tm) hexagonal microprism crystals: hydrothermal synthesis and luminescent properties," *Inorganic Chemistry*, vol. 46, no. 16, pp. 6329–6337, 2007.

[40] D. Shi, J. Lian, W. Wang et al., "Luminescent carbon nanotubes by surface functionalization," *Advanced Materials*, vol. 18, no. 2, pp. 189–193, 2006.

[41] A. O. Wright, M. D. Seltzer, J. B. Gruber, and B. H. T. Chai, "Site-selective spectroscopy and determination of energy levels in Eu^{3+}-doped strontium fluorophosphate," *Journal of Applied Physics*, vol. 78, no. 4, pp. 2456–2467, 1995.

[42] Y. K. Voronko, A. B. Kudryavtsev, A. A. Sobol, and E. V. Sorokin, *Spectroscopy of Oxides Crystals for Quantum Electronics*, Nauka, Moscow, Russia, 1991.

[43] J. Carpéna, L. Boyer, M. Fialin, J. R. Kiénast, and J. L. Lacout, "Ca^{2+}, $PO_{4_{3-}} \rightleftharpoons Ln^{3+}$, $SiO_4{}^{4-}$ coupled substitution in the apatitic structure: stability of the mono-silicated fluorbritholite," *Comptes Rendus de l'Academie de Sciences Serie IIa*, vol. 333, no. 7, pp. 373–379, 2001.

[44] R. El Ouenzerfi, G. Panczer, C. Goutaudier et al., "Relationships between structural and luminescence properties in Eu^{3+}-doped oxyphosphate-silicate apatite $Ca_{2+x}La_{8-x}(SiO_4)_{6-x}(PO_4)_xO_2$," *Optical Materials*, vol. 16, no. 1-2, pp. 301–310, 2001.

[45] Y. Lin, Z. Yang, and J. Cheng, "Preparation, characterization and antibacterial property of cerium substituted hydroxyapatite nanoparticles," *Journal of Rare Earths*, vol. 25, no. 4, pp. 452–456, 2007.